NANO · MICRO small
www.small-journal.com

Digital Detection of Single Virus Particles by Multi-Spot, Label-Free Imaging Biosensor on Anti-Reflective Glass

Giovanni Nava, Luca Casiraghi, Thomas Carzaniga, Giuliano Zanchetta, Marcella Chiari, Francesco Damin, Valentina Bollati, Lucia Signorini, Serena Delbue, Tommaso Bellini, and Marco Buscaglia**

Rapid detection of whole virus particles in biological or environmental samples represents an unmet need for the containment of infectious diseases. Here, an optical device enabling the enumeration of single virion particles binding on antibody or aptamers immobilized on a surface with anti-reflective coating is described. In this regime, nanoparticles adhering to the sensor surface provide localized contributions to the reflected field that become detectable because of their mixing with the interfering waves in the reflection direction. Thus, these settings are exploited to realize a scan-free, label-free, micro-array-type digital assay on a disposable cartridge, in which the virion counting takes place in wide field-of-view imaging. With this approach we could quantify, by enumeration, different variants of SARS-CoV-2 virions interacting with antibodies and aptamers immobilized on different spots. For all tested variants, the aptamers showed larger affinity but lower specificity relative to the antibodies. It is found that the combination of different probes on the same surface enables increasing specificity of detection and dynamic range.

1. Introduction

Quantifying the amount of a specific virus in biological samples is a fundamental process to manage an infection, as widely demonstrated during the SARS-CoV-2 pandemic.[1] However, despite the massive use of tests to detect virus components such as nucleic acids via quantitative real-time polymerase chain reaction (qRT-PCR) or surface proteins via lateral flow test (LFT) or enzyme linked immunosorbent assay (ELISA),[2,3] there is no method available to directly quantify the amount of whole viral particles in swab, saliva or exhalate samples. The current standard to attempt such quantification is based on incubation of cells with infected samples to be performed in specialized laboratory. The results are typically expressed in plaque forming units (PFU) per sample volume . However, the number of viral particles effectively needed to form a plaque in the cell plate can vary by orders of magnitude and strongly depends on the experimental conditions.[4] Despite the lack of methods suitable for massive diagnostic applications, various strategies have been developed to detect and enumerate single virus particles. This can be achieved by detecting the light scattered by virion particles. Flow cytometry instruments,[5] as well as custom designed optical virus counters, can enumerate virus particles in solution and discriminate them according to their size. With similar instruments, specificity to virus populations can be achieved by fluorescence labeling and detection.[6,7]

A different class of optical methods, combining virions counting and discrimination of specific virus type, relies on the binding of virus particles on specific molecular probes immobilized on a biosensor surface.[8] These technologies deal with the general problem of imaging nanoparticles (NP), whose size is smaller than the diffraction limit, without the use of fluorescent labels or other amplification means provided by additional reagents. The main strategies recently adopted for direct, label-free imaging of NP on surfaces are three:[9] (i) dark-field microscopy aims at reducing the background signal at the point that the weak intensity scattered by a single NP becomes directly detectable;[10] (ii) methods based on plasmonic or photonic resonances rely on spectral shifts of reflected or diffracted light upon NP binding;[11]

G. Nava, L. Casiraghi, T. Carzaniga, G. Zanchetta, T. Bellini, M. Buscaglia
Dipartimento di Biotecnologie Mediche e Medicina Traslazionale
Universitá degli Studi di Milano
via F.lli Cervi, 93, Segrate, Milano 20054, Italy
E-mail: tommaso.bellini@unimi.it; marco.buscaglia@unimi.it

The ORCID identification number(s) for the author(s) of this article can be found under https://doi.org/10.1002/smll.202300947.

DOI: 10.1002/smll.202300947

M. Chiari, F. Damin
Istituto di Scienze e Tecnologie Chimiche "Giulio Natta"
National Research Council of Italy (SCITEC-CNR)
via Mario Bianco 11, Milano 20131, Italy

V. Bollati
Dipartimento di Scienze Cliniche e di Comunitá
Universitá degli Studi di Milano
via S. Barnaba 8, Milano 20122, Italy

L. Signorini, S. Delbue
Dipartimento di Scienze Biomediche
Chirurgiche ed Odontoiatriche
Universitá degli Studi di Milano
via Pascal 36, Milano 20133, Italy

(iii) interferometric techniques provide an amplification of the signal of single NP by summing their scattered field to a reference field with controlled phase and amplitude obtained from a reflective interface.[12] However, all these technologies have important limitations. Dark-field microscopy can be affected by stray light and spurious signals when working with complex samples.[13] Plasmonic and interferometric methods applied to the detection of single dielectric NP can provide brighter images, hence less affected by artifacts, and can achieve large sensitivity and time-resolution, but typically require more complex set-ups with spectral or angular adjustment or laser-scanning.[14,15] Among (ii) and (iii), a few methods rely on simpler instrumental set-up, more suitable for a bench top diagnostic device, and also work in wide-field microscopy[16,17] and low magnification.[18]

In all these optical methods the sensitivity is proportional to the number of photons scattered by each NP and acquired by the system, which leads to the choice of optical designs with large enough collection angle (i.e., numerical aperture, NA) that brings about small field-of-view, small depth-of-field and the need for surface scanning and focus adjustment. Here, instead we show that in a wide field-of-view, small-NA condition, the loss of photons induced on the incoming light by single NP scattering can be exploited in a thin layer interferometric reflection scheme as a sensitive principle of detection. In other words, the signal of a NP binding on a reflective planar biosensor interface can be seen by a low aperture objective as a negative contribution to the reflected field carrying a phase delay corresponding to the NP-interface distance. Such regime, to our knowledge not yet explicitly formulated, overcomes two serious limitations affecting other methods: (i) it combines single NP detection with a wide field-of-view, thus maximizing the sensitive area in digital regime and enabling its implementation in micro-array format; (ii) it provides an optical scheme less sensitive to focus adjustment hence simpler and more robust.

We implemented this concept in an optical device using a simple scheme: LED illumination, common static optical components and a disposable plastic cartridge with a glass window glued on a wall and coated by a thin SiO_2 layer. The coated surface, which faces the inside of the cartridge in contact with an aqueous solution of choice, is spotted to form an array of antibodies and aptamers targeting spike protein of SARS-CoV-2. By processing the images formed upon collecting the LED light reflected by the coated surface, we could count single virions binding to the spotted receptors. In this digital (i.e., counting) regime, we can detect in a few minutes concentrations of virions as small as those needed for the much longer plaque forming assays based on cell cultures.

2. Results and Discussion

2.1. Principles of Digital Interferometric Reflective Phantom Interface

We achieve high sensitivity to the detection of single virion NP on a glass surface built to minimize the reflection in water. This is obtained by depositing a SiO_2 thin layer (of thickness h) on a Flint glass substrate of adequate refractive index to produce destructive interference in the reflection direction. This condition, achieved for $nh \simeq \lambda/4$, λ being the wavelength of the illuminating light and n the refractive index of the layer, is also a condition in which the reflected intensity becomes very sensitive to small changes of thickness.[19] The light scattered by a NP on the surface produces a local variation of the destructive interference, as sketched in **Figure 1**a, yielding a resolution-limited localized increase or decrease of the resulting reflected intesity. We name this single NP detection condition as "Digital Interferometric Reflective Phantom Interface" (DIRPI). Remarkably, the local variation of the reflected intensity is accessible even by low NA collection optics, thus extending single NP sensitivity to large field-of-view.

The optical scheme, sketched in Figure 1b, is based on a through-the-objective geometry, in which the light emitted by a narrow band LED source is focused on an off-axis position of the back focal plane of a 10x objective to obtain a slightly tilted collimated illumination on the anti-reflective sensor surface. The surface is treated with a multifunctional copolymer providing at the same time passivation and covalent linking of antibody and aptamers, which are immobilized in 50–100 µm-size spots. The glass chip has a slightly prismatic shape that enables singling out the reflection from the sensing surface, which propagates back into the objective along a direction different from that of the light reflected by the cuvette's plastic walls and is imaged on a CCD camera.

The collected light is composed by the plane waves reflected by the glass-SiO_2 and the SiO_2-solution interfaces (E_1 and E_2, respectively, nearly opposite in phase), and by the light back-scattered by the virion NP (E_{NP}) (see Figure 1a). The low NA of the collection optics poses us in a novel regime that can be described in the framework of the optical theorem,[20] where the total light extinguished by scattering or absorption by a small particle coincides with the forward interference between the incoming plane wave and the scattered field. For non-absorbing NP, this translates in having a (often overlooked) subtractive in-phase contribution in the scattered field proportional to the squared optical polarizability of the NP. As discussed by different approaches, this term originates from the radiation reaction effect on an oscillating dipole.[21–23] This condition is pictured in Figure 1c (top), where the forward interference results in a local decrease of amplitude of the propagating plane wave accounting for the scattering loss. The same terms are added in the backward direction to form the DIRPI signal. In this case, the distance between the virion and the SiO_2-solution interface adds a delay in the phase of the back-scattered field relative to the reflected plane wave E_2, as depicted in Figure 1c (bottom).

For the sake of clarity, we can represent the DIRPI condition by a phasor plot (Figure 1d), picturing the thin layer interference terms E_1, E_2 and $E_R = E_1 + E_2$, and the NP contribution as described above. These terms are represented in Figure 1d for the case $nh < \lambda/4$. Since E_2 has the same phase of the incoming wave, the field scattered by the NP would be opposite in phase (subtractive) for an ideal NP centered exactly at the interface, whereas it is further delayed (clockwise rotation) by a phase corresponding to the distance between the interface and the NP center (i.e., at least the NP radius). For NP with 100 µm diameter, this results in a E_{NP} term pointing approximately

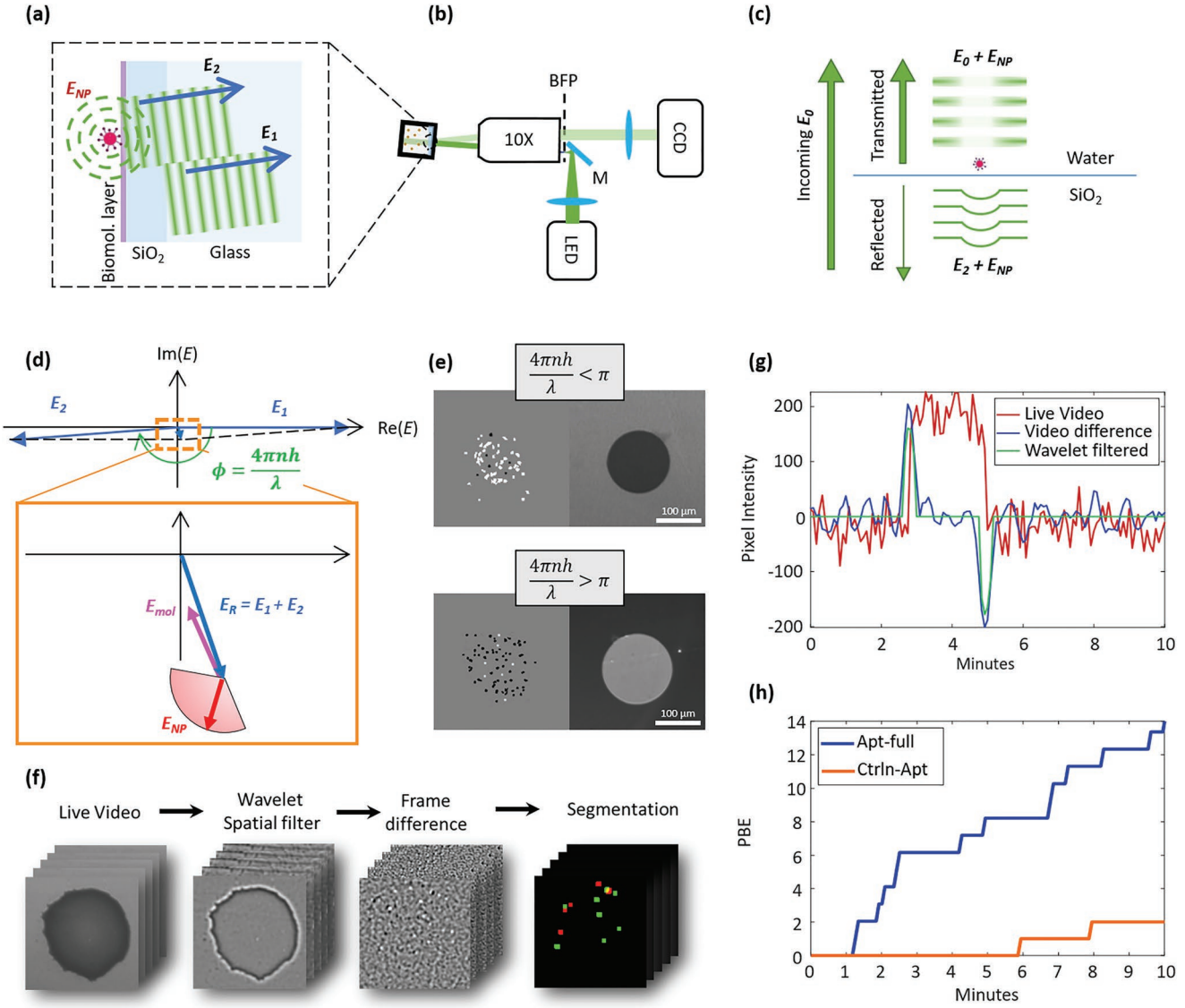

Figure 1. Diagram of the experimental setup and principle of DIRPI. a) Virion NP bind to antibody or aptamer probes spotted on the surface of a glass chip coated with an anti-reflective SiO_2 layer. The incoming field (propagating from right to left, not reported) is reflected by the two layer interfaces (E_1 and E_2), and is scattered by the NP (E_{NP}). b) Through-the-objective experimental geometry to reveal the binding events by recording the image of reflected light by a a CCD camera. The light of a LED source is reflected by a mirror (M), focused off-axis on the back focal plane (BFP) of a 10X objective, reflected by the sensor surface, and imaged on a CCD camera by the same objective and a lens. c) Schematic representation of the effect of a single NP on an incoming plane wave with field amplitude E_0 and on the plane wave reflected by a nearby interface. The conservation of energy implies that the field scattered by the NP (E_{NP}) induces a local decrease of amplitude of the transmitted field.[21] The same scattered field yields a local change of phase in the reflected field due to the delay introduced by the NP-interface distance. d) Phasor diagram representing the field E_1 reflected by the glass-SiO_2 interface, the field E_2 reflected by the SiO_2-solution interface, the resulting field $E_R = E_1 + E_2$, the contribution E_{mol} due to an increase of biomolecular layer (violet), and the additional term E_{NP} due to NP surface binding in the DIRPI configuration (red). e) Example of DIRPI analysis (left) and reflected intensity image (right) of an antibody spot during NP binding, for SiO_2 thickness smaller (top) and larger (bottom) then $\lambda/4$. f) The experimental live video are wavelet-filtered spatially to match the point-spread-function of the NP, a video-difference is then performed and a segmentation procedure permits to classify dark or bright events. g) Binding events (or unbinding) yield a sudden step-variation in the intensity of a pixel in time (red line), which is converted into a peak in frame-difference video (blue line). The peaks are further enhanced relative to the background using wavelet transform (green line). h) Particle binding events counted on spots of aptamer (Apt-full) and control DNA after addition of SARS-CoV-2 virions, Wuhan D614G variant, at 9.5×10^4 PFU mL^{-1}.

downward in the phasor plot of Figure 1d within an angle given by the fluctuation in the NP-interface distance. The combination of (i) similar phase and (ii) not too dissimilar amplitude of E_{NP} and E_R makes the scattering of the NP detectable as an intensity modulation.

Remarkably, the sign of the intensity modulation due to NP is opposite to that of a thin and uniform molecular layer deposited on the SiO_2-solution interface, such as the layer of antibodies and aptamers used to capture the virions. In the phasor plot (Figure 1d), the term due to the molecular layer

(E_{mol}) is in this case pointing away from E_R, since it corresponds to an increase of the effective thickness of the SiO_2 layer thickness and a consequent additional delay (clockwise rotation) of E_2.[19] The directions of the terms E_{NP} and E_{mol} remain the same even if $nh > \lambda/4$. In this case, E_R points upward in the phasor plot (not reported), and thus virions NP yield a negative signal and an increase of the molecular layer thickness a positive reflective signal. This effect can be appreciated in Figure 1e, where the digital signal from the virions (left) and the uniform signal from spotted antibodies (right) are compared side-by-side. We observed mostly bright single NP signals and dark spots of antibody (or aptamer) when nh is smaller than $\lambda/4$ (top), and bright spots and dark NP signals if nh is larger than $\lambda/4$ (bottom).

Thanks to the interferometric condition here adopted, particle binding or unbinding produce a small but detectable sudden variation of the intensity involving a small group of pixels in the acquired images, whose size equals the point spread function (PSF) of the collection system of size about 2.9 ±0.5 μm. Following this notion, the raw stack of images is processed using a step-detection algorithm exploiting space and time filtering with an "à trous" wavelet algorithm.[24] Figure 1f details the stages of such analysis, that connect the left and right-handed images in panel e. Raw images are first filtered in space with a wavelet function matching the size of the PSF in order to reduce the noise. Then a moving average is computed in time and a differential video is produced, so that every sharp step signal becomes a recognizable peak with defined width. The final step is a discrimination step in which values below a given threshold are removed. This is performed by filtering the time trace of each pixel with a wavelet function matching the time width of the peaks and also providing an optimal threshold for particle detection as described in [24]. The obtained stack of binary images undergoes a 3D (2D + time) particle detection algorithm, by which binding events are classified in time and space. Signals measured in the same position of a previous binding event but opposite in sign are identified as unbinding events. Figure 1g exemplifies the analysis as a function of time. A single pixel trace corresponding to a binding event followed by unbinding is shown as raw brightness values (red line), after spatial filtering and averaged frame difference (blue line), and after time filtering with the à trous wavelet algorithm and thresholding (green line). Overall, our analysis enables to pinpoint the binding events, which appear as positive and negative spikes of well determined size and duration, and the occurrence of their unbinding.

By exploiting this analysis, the average rate of particles binding on antibodies, aptamers and control spots is obtained by the simple counting of single events on each spot. This is shown in Figure 1h, where the cumulative number of particle-binding events (PBE), that is, step-like changes of optical signal detected by the analysis and associated to binding of a nanoparticle onto the surface, is plotted in time after a sample containing SARS-CoV-2 virions is added in a DIRPI cartridge at a concentration of 9.5×10^4 PFU mL^{-1}. As expected, the cumulative PBE grows with time. Since the virion concentration is much smaller than the typical equilibrium constants for molecular binding and the number of surface bound virions remains much smaller than the total virions in solution, the PBE is expected to grow linearly with time and the observed fluctuations are due to the statistics of the small number of discrete events detected. Therefore, the PBE rate can be simply estimated as the end-point cumulative PBE divided by the observation time. In the case of Figure 1h, the aptamer spot (blue) specifically recognizing spike protein yields 1.4 PBE min^{-1}, significantly larger than 0.2 PBE min^{-} measured on the control DNA spot (orange).

2.2. Assay Demonstration with Spike Protein-Coated Nanoparticles

We first studied the optical response of DIRPI upon surface binding of synthetic NP mimicking SARS-CoV-2 virions with the purpose of validating the detection scheme and the binding event discrimination capability for NP whose size, refractive index and surface structure were known to a better degree than virions. To this aim, we selected streptavidin-coated polystyrene nano-spheres (radius r = 50 nm) and functionalized them with biotin-conjugated HexaPro variant of spike protein (Note S1, Supporting Information). The resulting spike protein-coated NP were suspended in phosphate buffered saline (PBS) buffer and injected into the measuring cartridge to achieve concentrations, expressed as number of NP per mL, between 1.8×10^6 and 6×10^9 NP mL^{-1}. The sensor surface was prepared with spots of immobilized monoclonal antibody targeting the receptor binding domain (RBD) of SARS-CoV-2 spike protein (Ab-RBD). The resulting PBE was recorded over time.

To optimize the experimental conditions and the signal analysis, we performed binding experiments with different parameters choice around the ideal $nh = \lambda/4$ condition by changing either λ or h. **Figure 2**a reports DIRPI binary images of an Ab-RBD spotted surface in three different conditions: (i) a sensor surface with nh slightly thicker than $\lambda/4$ for blue light illumination (λ σσ 455 and h = 80 nm), which has been demonstrated to provide an optimal sensitivity to molecular binding over a large planar region,[19] and two alternative versions with a SiO_2 layer significantly thinner than $\lambda/4$, obtained either by (ii) a larger wavelength (λ = 530 and h = 80 nm) or (iii) a thinner SiO_2 layer (λ = 455 and h = 70 nm). The corresponding distribution of local brightness increase of the recorded PBE is reported in Figure 2b. Figure 2a,b shows that in case (i) the number of negative events yielding brightness decrease (black dots) is slightly larger, while in (ii) and (iii) positive events (white dots) dominate, their total number being larger in (ii) than in (iii). The distribution of the number of pixels corresponding to a detection event in all these conditions is shown in Figure 2c, with peak values in the range 4–6 pixels, corresponding to 5–8 μm, slightly larger hence compatible with the PSF of the low NA of the optical system designed to privilege a wide field of view.

Given the larger number of positive counts and the smaller pixel area of binding events, we selected the condition (ii) for the studies on real virus detection. In this condition, the contrast of the NP binding signal, defined as the ratio between the maximum brightness increase and background brightness, is 1.1±0.4%. This value is coherent with the computed scattering cross section of the particles and the observed PSF (Note S2, Supporting Information).

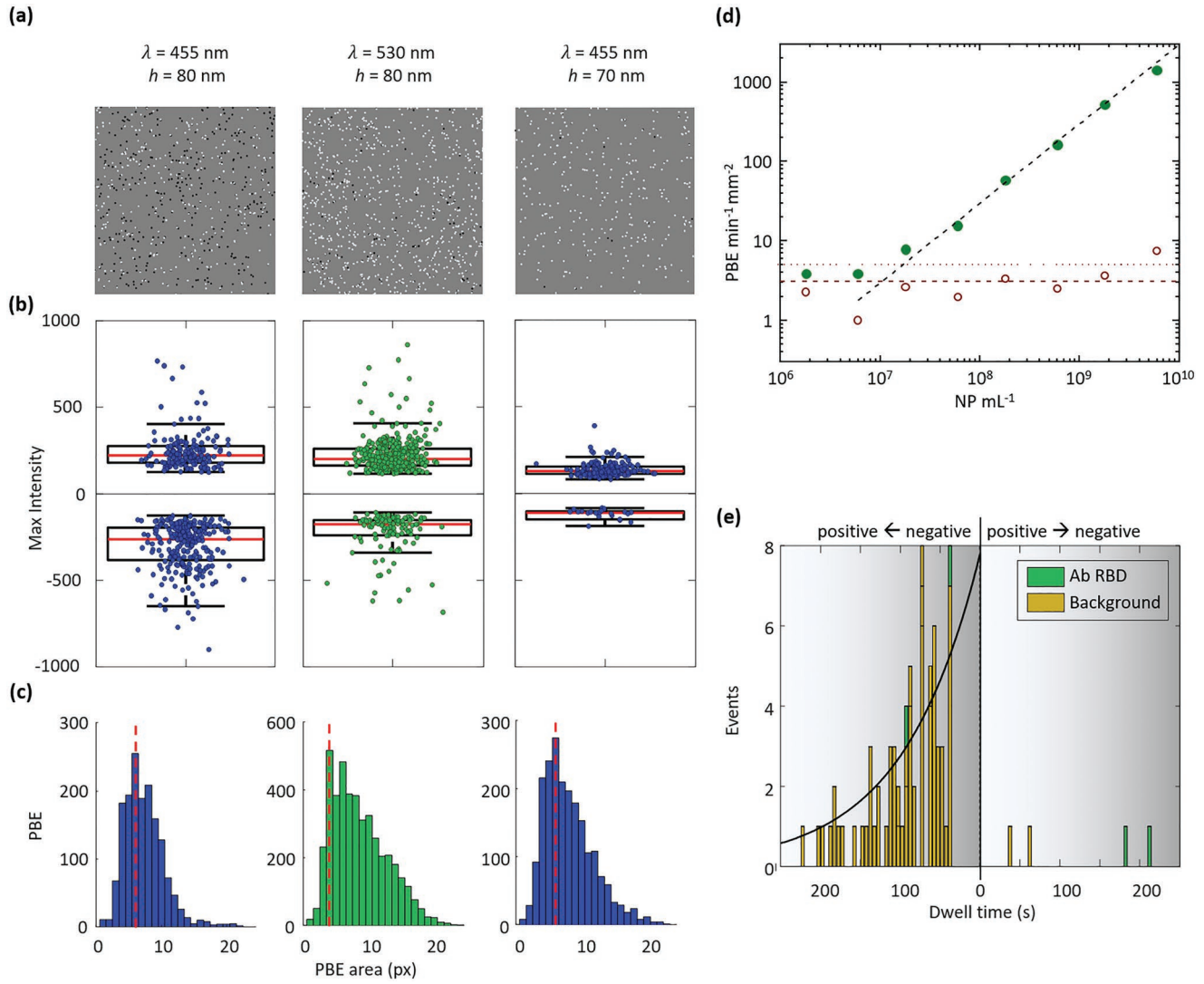

Figure 2. Validation of DIRPI with spike protein-coated nanoparticles. a) DIRPI images of a surface region with immobilized anti-spike antibody acquired after addition of polystyrene NP decorated with SARS-CoV-2 spike protein, obtained with different combination of illumination light wavelength λ and SiO_2 thickness h, as indicated: blue light and $h = 80$ nm (left panel), green light and $h = 80$ nm (center panel), blue light and $h = 70$ nm (right panel). White (black) dots indicate a local increase (decrease) of reflected intensity. NP concentration is 6×10^7 NP mL^{-1} and the acquisition time is 25 min. b) Box plot of the maximum pixel brightness for each PBE acquired during the measurements of panel a expressed in grey levels of the 16 bits image depth. Red lines indicate median values, the bottom and top edges of the box indicate the 25th and 75th percentiles, respectively. The whiskers extend to the most extreme data points not considered outliers. The ratio between the number of positive and negative PBE is 0.65 (left), 3.19 (center) and 7.42 (right). c) Pixel area distribution of all the PBE of panel a and b. Vertical red dashed lines indicate the peaks positions. In panels b and c, the left, center and right plots refer to λ and h values of the corresponding image of panel a. d) Rate of PBE measured on spot of anti-spike protein antibody (green) and background PBE on copolymer coating (red) for increasing concentrations of spike protein-coated NP. The black dashed line represents a linear fit to the green data points for NP concentration larger then 10^7 NP per mL. The red dashed (dot) line represents the average value (standard deviation) of the red data points. Illumination wavelength and SiO_2 thickness are $\lambda = 530$ and $h = 80$ nm, respectively. Each data point is obtained with an acquisition time of 25 min. e) Distribution of dwell times Δt observed for two co-localized consecutive events with positive and negative intensity change during the measurement of panel (d). The left (right) side reports the dwell time for a negative (positive) signal followed by a positive (negative) one. The black curve represents an exponential fit to the negative values of Δt yielding a characteristic time of 96 s.

The scaling with concentration of the binding rate of NP on a surface measured in digital regime is still controversial in the literature. Logarithmic[25] or power law[26] dependencies have been reported for NP counting in the concentration range from 10^5 to 10^9 NP mL^{-1}. We studied the concentration dependence of the rate of spike protein-coated NP surface binding events measured by DIRPI. As shown in Figure 2d, an ideal linear scaling is obtained when the measured rate is larger than 10 binding events in a mm^2 per minute, corresponding to about one binding event every 10 min in each spot. Such level represents the background noise in the chosen experimental condition and for the image processing parameters. The observed linear dependence with concentration is consistent with a simple Langmuir model for binding as commonly found

in molecular biosensors for concentrations much lower than K_d,[27] in which mixing of sample is efficient and rapid, particle enumeration is not limited by data processing and the molecular interactions between probe and target are independent and monovalent. Therefore, the observed behavior indicates that such conditions are met by DIRPI.

The study of spike protein-coated NP binding on surface immobilized Ab-RBD enables to estimate the accessible dynamic range of DIRPI. Figure 2d shows that a linear scaling with concentration is maintained from 10 up to 10^3 PBE min^{-1} mm^{-2}. An upper limit in the linear scaling is expected in a condition of very large PBE rate, when the probability of multiple NP binding occurring in close proximity in space and time becomes significant. Consecutive binding events within the spatial and time resolution of the analysis are counted as a single NP, hence leading to deviation from the linear scaling with concentration. Figure 2d demonstrates that such limit is larger than 10^3 PBE min^{-1} mm^{-2} in the current configuration. The concentrations of spike protein-coated NP corresponding to the observed linear range are between 10^7 and 10^{10} NP mL^{-1}. Such concentrations cannot be simply translated to the detection capability of real virions by Ab-RBD because of the different number of spike proteins (about 10 per NP in the virus mimics, much less than in real virions). Moreover, spike protein-coated NP are not suitable to characterize the binding by aptamers, because biotin conjugation of Hexapro spike protein, required for the production of spike protein-coated NP, inhibits the binding to surface immobilized aptamers. This is shown by ensemble molecular binding experiments performed on spike protein by Reflective Phantom Interface (RPI) label-free biosensor[19] on a similar measuring cartridge (Figure S1, Supporting Information).

A fraction of NP binding events is eventually followed by unbinding, depending on the type of interaction and its dissociation rate constant. Figure 2e shows the dwell time distribution measured during the experiment reported in Figure 2d. Remarkably, we could detect co-localized consecutive signals with opposite signs only when the first event is associated to a negative intensity change, and they are mostly located in the surface region surrounding the spotted probes. About 8% of the NP detected outside the spots unbind within 5 min after binding and the dwell time distribution is compatible with an exponential behavior with a decay time of 96 s. Only very few unbinding events are detected inside the antibody spot, and they follow a positive intensity increase, as shown in 2e. We interpreted this observation as a stable, long-lasting binding of spike protein-coated NP on antibody spots. In contrast, the observed negative binding signal outside the spot are interpreted as non specific binding occurring at a larger distance from the surface,[28] possibly mediated by adsorbed contaminants or protrusions of the surface copolymer coating.

2.3. Digital Detection of SARS-CoV-2 Single Virions

We used DIRPI to detect different variants of SARS-Cov-2 virions in a concentration range spanning common diagnostic conditions. As specific molecular probes we chose Ab-RBD antibody and two aptamers binding the spike protein of the virus. Apt-RBD aptamer binds the RBD of spike protein[29] similarly to the antibody, whereas Apt-full aptamer does not bind the RBD, but other regions of spike protein.[30] The binding of SARS-CoV-2 spike protein in solution with the selected probes immobilized on the biosensor surface was preliminary tested by RPI analysis (Figure S2, Supporting Information).[31,32] The measured equilibrium dissociation constants K_d for all the probes are in the range 0.5–60 nM. However, diagnostically relevant concentrations to evaluate the infectivity of a subject are typically many orders of magnitude lower. This concentration regime, much lower than the K_d of the probes, is exactly the field of application for digital biosensors like DIRPI that count single binding events, hence achieving ultrasensitivity.[8]

The biosensor surface spotted with specific probes and controls is shown in **Figure 3**a. Experiments were conducted in a biosafety level 3 (BSL-3) laboratory. To this aim a compact and autonomous version of the DIRPI instrument was designed to be mounted in a BSL-3 hood. Virus samples obtained from cell culture and quantified by both qRT-PCR and plaque forming assay were added in the DIRPI cartridge at increasing concentrations. Figure 3b shows an example of the single binding events detected on the biosensor surface within 20 min from the addition of Delta variant at a concentration of 1.5×10^3 PFU mL^{-1}. Single binding events are enumerated in time for each spot (Figure 3c) showing a rapid and monotonous growth of PBE mm^{-2} for both antibody (green line) and aptamers (blue and cyan lines). As expected, control spots displayed much lower values of PBE.

The enumerated binding events were analyzed in terms of pixel area, intensity and dwell time distributions (Figure S3, Supporting Information). Both the distributions of pixel area and intensity of PBE are similar although slightly narrower than those obtained for spike protein-coated NP (Figure 2b,c). Comparing the PBE intensity of different spots, a small difference is observed between antibody and aptamers: the measured intensity change due to virus binding on Ab-RBD is smaller. We interpret this behavior as an effect of the different distance between the virion particle and the SiO_2 interface due to a larger size and more rigid structure of the antibody molecule. Similar behaviors were also observed for Wuhan D614G (Supplementary Figure 4) and Omicron (Supplementary Figure 5) variants.

We then studied how the PBE rates depend on virion concentration and virus variant. The results are summarized in Figure 3d–i, showing PBE rates on antibody (panels d-f) and aptamers spots (panels g-i) as a function of the amount of virus present in the cartridge expressed as a function of threshold cycles of qRT-PCR (CT, bottom x-axes). These observations are performed for the Wuhan D614G (panels d and g), Delta (panels e and h) and Omicron variants (panels f and i), as marked in the legends. We observed responses that markedly depend on both receptor type and virus variant.

We found that the three variants yield different DIRPI counts for similar nominal concentrations expressed in CT. Figure 3d–i also indicate the values of PFU mL^{-1} measured by plaque forming assay (top x-axis). Remarkably, the three variants display very different ranges of PFU mL^{-1} for similar PBE and the two measured values of PFU mL^{-1} and CT scale differently with one another for the three variants. We found

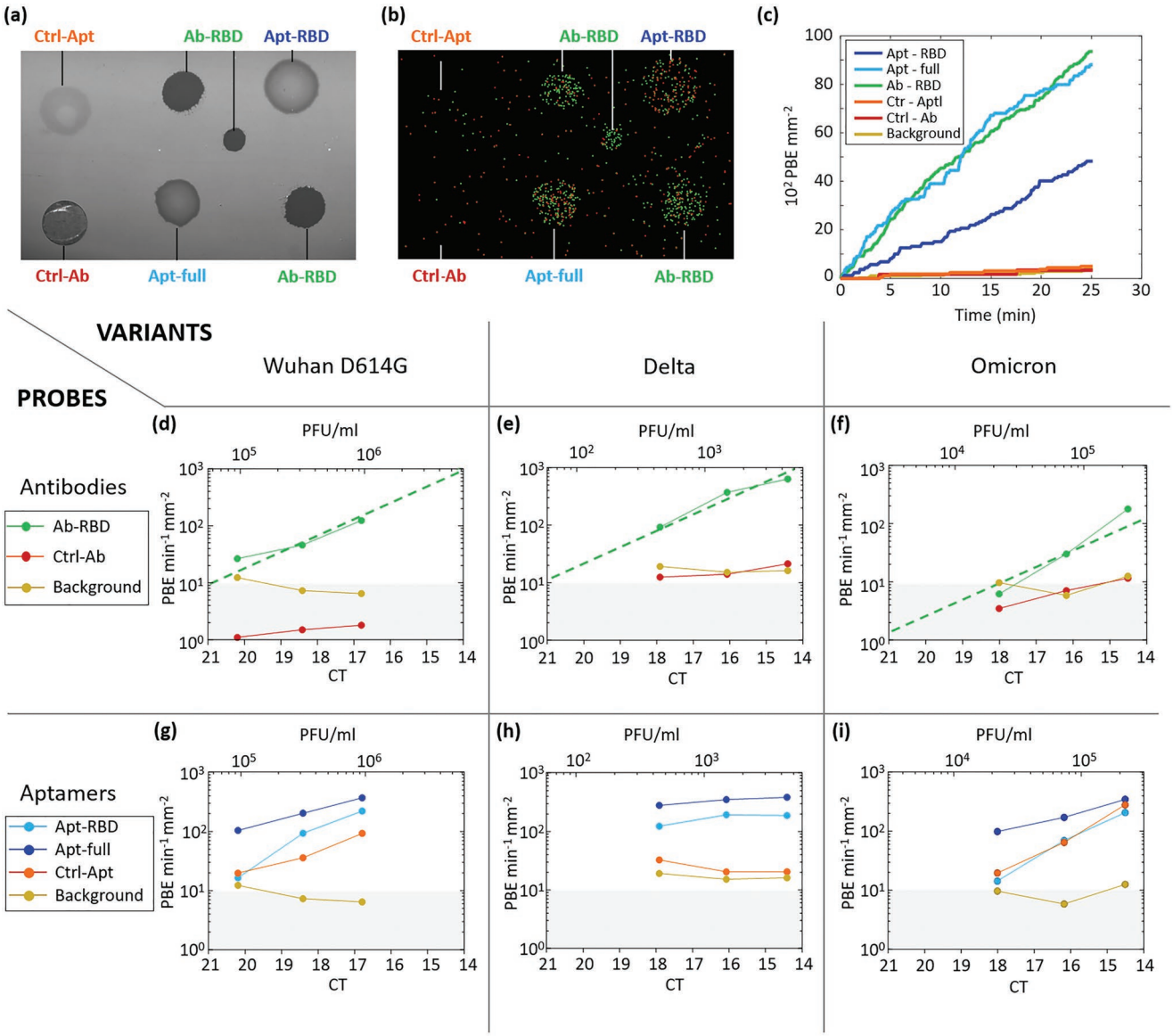

Figure 3. Digital Detection of SARS-CoV-2 single virions. a) RPI image of the sensor surface with spots of antibody and aptamers targeting spike protein and control spots, as indicated. b) DIRPI image of the sensor surface of panel a showing detected PBE during a 25 min observation time in presence of 1.49×10^3 PFU mL^{-1} of Delta variants virions. Green (red) dots represent PBE associated to positive (negative) intensity change. c) Cumulative PBE per mm^2. The values are reported in units of 10^2 PBE mm^{-2} to approximate the corresponding counting on a single spot. d–i) PBE rate per mm^2 measured on antibody (d–f) and aptamers (g–i) spots for different concentrations of Wuhan D614G (d,g), Delta (e,h), and Omicron (f,i) variants of SARS-CoV-2 virions. Colors refer to different spot types as indicated in the legends. The gray areas correspond to PBE min^{-1} mm^{-2} $\leqslant$ 10 assumed as a threshold for a significative signal.

the PBE rate values we measured with DIRPI to be more consistent with the CT axis. The larger variation of the PFU mL^{-1} values are ascribed to the different infectivity of the variants in the plaque assays, as observed in previous works.[4] We emphasize that since CT measures the amount of genome copies, PFU measures the number of virus capable of infecting a cell, and DIRPI directly measures the number of intact virions, these three approaches, though correlated, provide complementary information, as discussed below.

Figure 3d–i shows that both antibody and aptamers spots provide event counts increasing with concentration for the three variants. In the case of Ab-RBD spots (panels d-f, green dots), PBE rates show a nearly linear growth with concentration (dashed green line), in agreement to what observed for spike protein-coated NP (Figure 2d). In the case of aptamer Apt-full (panels g-i, blue dots and line) we observed larger signals in most of the concentration conditions, but a weaker than linear scaling of PBE rate with concentration. The binding of SARS-CoV-2 virions to antibody and aptamers also differs in the control spots: while antibody control spot (red dots and line in panels d-f) shows counting compatible with background noise (yellow dots and line), that represents the number of spurious

events measured on the copolymer coating, and nearly independent on the virus concentration, the aptamer control spot (orange dots and line in panels g-i) captures a relevant amount of virions indicating the presence of a nonspecific component in the aptamer-virion interaction. The lower specificity of aptamers is also confirmed by the response to the presence of Herpes Simplex Virus-1 (HSV-1) particles observed in control measurements (Figure S6, Supporting Information). The capacity of DIRPI to detect virus particles in real matrices was confirmed by measurements performed on swab samples (Figure S7, Supporting Information). In this case, Ab-RBD, which was developed for early variants of SARS-CoV-2, could not capture efficiently the virions of the later Omicron subvariant. However, Apt-full spot indicated a positive response providing a large PBE rate signal, much larger than the case of the control HSV-1. These observations indicate that aptamer spots can provide less specific, but more sensitive response compared to Ab-RBD spot. In general, the binding efficacy of aptamers on a surface can depend on the immobilization conditions. The copolymer coating used for the surface immobilization and the poly-A spacer (see Experimental Section) grant conformational flexibility to the aptamers. The surface density of aptamer spots was quantified from the spot contrast of the RPI reflective image[19] obtaining $4(\pm 0.5) \times 10^{12}$ molecules cm^{-2}. This can be considered an intermediate value of surface density, around which a maximum efficiency of binding for protein target has been reported.[33] In principle, an accurate optimization of the immobilization conditions of Apt-full and Apt-RBD at lower surface densities can lead to increased specificity, although at the cost of a possible reduction of sensitivity.

The linear behavior of SARS-CoV-2 virions binding to Ab-RBD, makes PBE counting a direct measure of the viral concentration, whose Limit Of Detection (LOD) is given by the condition in which the specific binding rate equals the non-specific one. This can be estimated for the three virus variants as the concentration at which 1 PBE is detected in a single spot of Ab-RBD for 10 min observation time, corresponding to about 10 PBE min^{-1} mm^{-2} on a spot with a diameter of 100 µm. We thus computed the LOD as the extrapolated concentration yielding 10 PBE min^{-1} mm^{-2} for the three variants. The obtained LOD is CT 20.9 (5.7×10^4 PFU mL^{-1}), CT 21.2 (51 PFU mL^{-1}) and CT 18 (2.2×10^4 PFU mL^{-1}), for Wuhan D614G, Delta and Omicron, respectively. Remarkably, the values of LOD expressed in CT and in PFU mL^{-1} display different behaviors. The large difference observed for the LOD of the three variants in terms of PFU mL^{-1} can have two different sources: different PFU per particle ratio in the plaque forming assay, or binding performance of the surface probes that depends on the virus variant. As shown in Figure 3d–e, considering the binding to Ab-RBD, we observed that Wuhan D614G and Delta variants provided almost the same counting for the same CT value (e.g., they both provided about 10 PBE min^{-1} mm^{-2} at CT 21). In this case, we can ascribe the different LOD in PFU mL^{-1} to different PFU per particle ratio in the plaque forming assay, hence leading to a value 10^3 times larger for such ratio in the case of Whuan variant. In contrast, for the Omicron variant (Figure 3f), the virion counting is much smaller at all CT values, therefore, the lower LOD is mainly ascribed to a smaller binding efficiency of Ab-RBD for such variant, as also confirmed by the weaker binding between Ab-RBD and Omicron RBD protein measured by RPI (Figure S8, Supporting Information).

Because of its non-linear and less specific response, binding to Apt-full is less prone to be directly used in SARS-CoV-2 virus concentration measurements. However, the larger binding capacity of Apt-full can be exploited by the multiplexing capability of our approach to strengthen the detection by Ab-RBD at concentrations close to the LOD, where interactions to Apt-full can offers a confirmation of the presence of virus particles.

Optical label-free biosensors have become standard tools to investigate biomolecular interactions thanks to their large sensitivity and the capability of measuring binding kinetics in real-time.[8] In the most standard (non-digital) design, the molecular binding signal is averaged over a sensor surface much wider than the optical resolution, from a single spot of 50-200 µm width,[31,32] up to cm-long channels.[34] A larger sensor area displaying a uniform composition of the bio-recognition layer enables better data averaging and thus larger sensitivity. In digital detection we look for highly localized signals, the opposite of averaging the signal. Indeed, if the virion binding signals were to be averaged on the whole sensor, the signal would be orders of magnitude below the background noise (Figure S9, Supporting Information). However, also the digital regime benefit from a large sensing area, which yields proportionally larger number of counts. DIRPI set-up achieves a large observation area by using a low-magnification, wide field-of-view objective. This also brings the advantage of multiplexing capability through different spot types measured at the same time. Therefore, larger spots would provide larger sensitivity, but fewer spots would affect the robustness and the specificity of the measurement. Accordingly, the spot size and number was selected as a compromise between these criteria.

A relevant feature of digital detection is to be largely unaffected by spurious signals originating by a complex sample matrix that would easily disrupt the measurement in an ensemble method. This is because, while non-specific interactions at molecular scale and small changes in buffer conditions can provide drifts in the averaged signals that are hardly distinguishable from specific binding (Figure S9, Supporting Information), analysis of localized binding events provides an intrinsic rejection of any signal that is on a larger scale than the PSF.

Overall, the image analysis enabling detecting single virions provides a larger set of characterization parameters than those available in ensemble approach. As described above, digital detection is the outcome of an analysis of intensity, size, stability and duration, where each of these parameters is exploited to discriminate between surface binding of virus particles and spurious effects. Discrimination of specific virus binding events is granted by DIRPI through multiple criteria: (i) the binding to different specific probes (i.e., antibody and aptamers); (ii) the passivation of the biosensing surfaces by antifouling copolymer coating; (iii) the presence of negative control spots to evaluate the non-specific signal; (iv) binding events with dwell times smaller than 15 s are filtered out by moving-average window; (v) binding events are further filtered according to contrast and area to improve the selectivity. As such, each of those is a control parameter to refine detection in the various conditions. In the case here reported of detection of SARS-CoV-2 virions

obtained from cell culture, we showed that the analysis can reduce the background noise down to the order of one spurious event per spot during an acquisition time of 10 min.

The contrast of the intensity signal measured upon single virion binding is typically between 0.5% and 1% for all SARS-CoV-2 variants, nasal swab sample and HSV-1, and is slightly smaller than the contrast observed for spike protein-coated NP (Figure S10, Supporting Information). The repeatability of the contrast offers the opportunity to further filter the PBE signal to discard additional possible spurious events with anomalous intensity, should this be necessary as for example when dealing with samples in a complex matrix. Indeed, for swab samples, the background counts can vary from sample to sample from 1 up to 10 per spot in 10 min (Figure S7, Supporting Information).

In principle, an improved selection of virus binding events can also be obtained by the analysis of dwell time distributions, as predicted by theoretical models.[35] Our analysis of SARS-CoV-2 binding events offers an example of how this could take place. Since we observed several unbinding events only outside the spot regions and associated to a negative first PBE signal we could interpret short lifetimes of the bond as associated to non-specific, incorrect binding occurring at a larger surface distance[28] and we could apply an additional filter on dwell time, which in our case was not necessary.

Our analysis enlightens the remarkable difference in viral load quantification obtained with different assays. This is relevant since viral loads are known to be associated with disease severity and mortality.[36] CT values measured by qRT-PCR typically are found in the range from 9, indicating the presence of very high viral load in the sample, to 37, indicating very low viral load, but different assays can provide very different values for the same sample.[37] Moreover, plaque forming assays are largely affected by the choice of cell type and we found that the results largely depend on virus variant. Therefore, CT values and PFU mL^{-1} generally provide complementary information, but neither detects the amount of virions directly. The direct virion counting offered by DIRPI completes the characterization of the sample in terms of viral load. Direct whole virus quantification also enhances the ability to determine the actual infectious capacity without the limitations of qRT-PCR, which cannot distinguish between intact virions and RNA fragments that may persist for weeks after the end of the infective phase.

3. Conclusion

A few label-free biosensor schemes have been recently proposed to detect and enumerate single virions. Total internal reflection dark field microscopy on glass based on laser illumination enabled counting of single influenza viral particles with a LOD of 10^4 PFU mL^{-1}.[38] A photonic crystal label-free biosensor was exploited to detect pseudotype SARS-CoV-2 virus particles with a LOD of 10^3 copies per mL.[39] Reflectance interference imaging on silicon has been demonstrated for discriminating between different viruses according to their signal[40] and for the detection of modified vesicular stomatitis viruses on DNA spots down to 100 PFU mL^{-1} after incubation with antibody-DNA conjugate in solution.[41] All these methods take advantage of high magnification objectives to acquire a large amount of light scattered by the virions, therefore they provide a small field-of-view acquisition. In contrast, we demonstrated that DIRPI provides at the same time digital detection and wide field of view, enabling scan-free multi-spot acquisition, all with a cost-effective optical set-up based on LED illumination and disposable glass/plastic cartridges. Such choice in the experimental design was aimed to bring DIRPI toward a scalable demonstrator device. As a matter of fact, one advantage of a "cartridge" approach, based on a single-use plastic couvette hosting the glass sensor (Note S11, Supporting Information), is that, unlike microfluidic based approach, the open cartridge does not suffer of clogging and does not need stages of purification or filtering of raw samples (e.g., nasal swab); even more so, it is prone to be used in a non-specialized laboratory by means of a simple pipette to add the sample. In our vision, DIRPI devices open the possibility to point-of-care quantitative diagnostic platforms filling the gap between easy-to-use rapid tests (LFT) and sensitive but labor intensive PCR-based assay. The combination of digital detection and micro-array format increases the accessible measuring parameters, not only by providing multiple negative control signals and distinct testing, but also through the use of various molecular probes yielding different degrees of specificity and sensitivity on the same particle. Here we showed that aptamers specifically designed to recognize different domains of spike proteins of SARS-CoV-2 displayed large capturing capability but low specificity (Figure 3g–i; Figures S3–S7, Supporting Information), suggesting a relevant role of electrostatic attraction of virions. Therefore, aptamers spots can provide a positive response at extremely low concentration of virions, but also relevant PBE rates for other types of virus (Figure S6, Supporting Information). In contrast, antibody recognition displayed excellent specificity, but larger LOD. Moreover, Ab-RBD displayed decreased binding capability for Omicron variant, whereas the aptamers maintained their discrimination capacity, especially at lower virion concentrations. In practice, the combination of the two classes of probes enables extending the dynamic range of the detection system and provides a predictable scale of specificity that increases with the measured concentration. Further improvements of LOD are expected by molecular probes with enhanced binding kinetics and by fluidic and mixing designs increasing the transport of NP onto the sensing surface.

4. Experimental Section

Preparation of DIRPI Sensor.: Wedge-like glass chips (F2 optical glass, Schott) with 5° angle, with maximum thickness of 2 mm and a size of 8 mm × 12 mm, were coated with SiO_2 to form an anti-reflection layer of 70 nm or 80 nm. After plasma cleaning, the chips were dip-coated with a copolymer of dimethylacrylamide (DMA), N-acryloyloxysuccinimide (NAS), and 3-(trimethoxysilyl) propyl methacrylate (MAPS)–copoly (DMA–NAS–MAPS) called MCP2 as described in [42]. Droplets of spotting buffer (Na_2HPO_4, pH 8.5, 150 mM and sucrose monolaurate 0.01% w/v for aptamers and PBS1X, Trehalose 50 mM for antibodies) containing probes at concentrations of 10 µM for aptamers and 1 mg mL^{-1} for antibodies, were deposited on the chip surface by an automated, noncontact dispensing system (sciFLEXARRAYER S5; Scienion AG, Berlin, Germany) in spots of about 100 µm diameter. The unreacted N-hydroxysuccinimide residues were blocked with a solution of 5% ethanolamine in Tris–HCl buffer and washed with water. Mouse

IgG monoclonal antibody anti-spike RBD (Ab-RBD), SARS-CoV-2 strain Wuhan-Hu-1, clone HL1003, was obtained from GeneTex (Irvine, CA USA product code GTX635792-01). A mouse IgG monoclonal antibody anti-Human IL-8 obtained from PeproTech (London, UK product codes 500-M08) was used as negative control (Ctrl-Ab). RBD aptamer (Apt-RBD, sequence: AAAAAAAAAAAACAGCACCGACCTTGTGCTTTGGGA GTGCTGGTCCAAGGGCGTTAATGGACA called CoV2-RBD-1C aptamer) was described in Song et al.[29] and full-spike aptamer (Apt-full, sequence: AAAAAAAAAAGATATCAACCCATGGTAGGTATTGCT TGGTAGGGATAGTG-GG CTTGATGTT called SP6.51 aptamer) was described in Schmitz et al.[30] A single strand sequence with minimal secondary structure was used as aptamer negative control (Ctrl-Apt, sequence: AAAAAAAAAATGAAATGTTGGAAGGGTCGGAGGACAGTCCTCCGGG TGGTATAG). The strands were modified at the C6 carbon of the 5′ terminal with amine in order to react with and covalently bond to NAS on the copolymer surface coating. DNA probes were purchased from Integrated DNA Technologies (Leuven, Belgium) with high-quality Ultramer synthesis.

DIRPI Measurements.: DIRPI measurements were performed using the apparatus and the analysis algorithm described in this paper. The sensor cartridges (Figure S11, Supporting Information) were filled with 1.0 mL of measuring buffer (PBS 1X, Tween 20 2% v/v, Sodium Azide 2% w/v). The cartridges were kept at room temperature during the measurement and a magnetic stirring bar rotating at 30 Hz ensured efficient mixing of the solution.[31] Sample injections of purified SARS-CoV-2 virus (Wuhan D614G and variants), HSV-1 virus and spike protein-coated NP were performed by adding a suitable volume of measuring buffer containing different amounts of target virus or NP to reach the desired final concentration in the cartridge. DIRPI measurements on real virus samples were performed in a BSL3-hood.

Image Processing for Digital Signal Extraction.: The 16-bit monochromatic frames were averaged on-board by the camera (32 or 64 averages) and transmitted to a computer every 5 s to obtain a measurement image stack. The frames were registered for mechanical translational movements using SIFT algorithm on ImageJ.[43] Subsequently, the images were processed using a Matlab custom code. Initially, the frames were wavelet-transformed in space with a wavelet compatible with the actual PSF of the optical system (being the NP smaller than the optical resolution); then, to detect the step-like events, video difference between two averaging windows moving in time was computed. After such procedure a step-like feature in time, representing a particle binding event, became a less-noisy local triangular peak. The obtained differential images stack was then filtered in time with an "à trous" wavelet algorithm[24](Figure 1f,g) and at the same time an intensity threshold was extracted. The thresholded binary image stack was then processed using a standard 3D particle analysis algorithm to filter out unwanted events on the basis of the particle geometry in space and time (circularity, convexity, size) and event duration. Finally, the detected events are accounted for on the basis of arrival time and place (i.e., specific spot, control spot, background) th us obtaining the particle trace counts (Figure 1h).

Viruses.: SARS-CoV-2 viral strains B.1 (Wuhan D614G- GISAID accession: EPI_ISL 584048), B.1.617.2+Ay.x (Delta- GISAID accession: EPI_ISL 7698448) and B.1.1.529-BA1 (Omicron- GISAID accession: EPI_ISL 15191983) were isolated from COVID-19 patients' nasopharyngeal swabs,titrated by plaque assay and sequenced by Next Generation Sequence system, as previoulsy described.[44] Herpes Simplex Virus type 1 (VR-733) was purchased from the American Type Culture Collection (ATCC; Rockville, MD, USA), propagated and titrated by plaque assay.

Supporting Information

Supporting Information is available from the Wiley Online Library or from the author.

Acknowledgements

The authors thank Anton Schmitz and Günter Mayer for the generous gift of the HexaPro Spike protein. This work has received funding from Ministero dell'Universitá e della Ricerca through grants FISR 2020 COVID, "VIAEREA" project no. FISR2020IP_04633, and PRIN 2017, project no. 2017Z55KCW. L.C. was supported by a young scientist fellowship from the UNIMI GSA-IDEA project.

Open Access Funding provided by Universita degli Studi di Milano within the CRUI-CARE Agreement.

Author Contributions

G.N. and L.C. contributed equally to this work; T.B., V.B., S.D., and M.B. designed the study; G.N. designed the optical setup; G.N., T.B and M.B. developed the optical model; L.C and G.N. constructed the experimental setup; G.N. developed the analysis method; T.C., L.C., F.D., and M.C. functionalized the chip surface; L.C. and T.C. designed the experiment; L.C. performed the experiments with the help of L.S. to test viruses; S.D. provided virus samples and BLS3 laboratory; L.C. tested the analysis method; T.C. and G.Z. designed and prepared the spike protein-coated nanoparticle; L.C. analyzed and visualized data; G.N., L.C., T.C., T.B., and M.B. wrote the manuscript and prepared figures with input from all of the authors.

Conflict of Interest

The authors have no conflicts of interest to declare that are relevant to the content of this article.

Data Availability Statement

The data that support the findings of this study are available from the corresponding author upon reasonable request.

Keywords

antibody, aptamers, digital detection, infectious diseases, label-free biosensors, nano-particles, viruses

Received: February 2, 2023
Revised: March 21, 2023
Published online:

[1] O. Vandenberg, D. Martiny, O. Rochas, A. van Belkum, Z. Kozlakidis, *Nat. Rev. Microbiol.* **2020**, *19*, 171.
[2] L. Falzone, G. Gattuso, A. Tsatsakis, D. Spandidos, M. Libra, *Int. J. Mol. Med.* **2021**, *47*, 6.
[3] A. Mane, S. Jain, A. Jain, M. Pereira, A. Sirsat, G. Pathak, V. Bhoi, S. Bhavsar, S. Panda, *Sci. Rep.* **2022**, *12*, 1.
[4] W. McCormick, L. A. Mermel, *Virol. J.* **2021**, *18*, 92.
[5] M. M. Bonar, J. C. Tilton, *Virology* **2017**, *505*, 80.
[6] S. Faez, Y. Lahini, S. Weidlich, R. F. Garmann, K. Wondraczek, M. Zeisberger, M. A. Schmidt, M. Orrit, V. N. Manoharan, *ACS Nano* **2015**, *9*, 12349.
[7] Z. Szakács, T. Mészáros, M. I. de Jonge, R. E. Gyurcsányi, *Nanoscale* **2018**, *10*, 13942.
[8] G. Nava, G. Zanchetta, F. Giavazzi, M. Buscaglia, *Nanophotonics* **2022**, *11*, 4159.

[9] L. Priest, J. S. Peters, P. Kukura, *Chem. Rev.* **2021**, *121*, 11937.
[10] S. Chen, Z. Huang, C. Liu, S. Yang, Y. Zhang, J. Sun, J. Chen, J. Chen, F. Xu, Y. Chen, Y. Fang, *Sens. Actuators, B* **2022**, *355*, 131317.
[11] Y. Zhuo, H. Hu, W. Chen, M. Lu, L. Tian, H. Yu, K. D. Long, E. Chow, W. P. King, S. Singamaneni, B. T. Cunningham, *Analyst* **2014**, *139*, 1007.
[12] G. Young, P. Kukura, *Annu. Rev. Phys. Chem.* **2019**, *70*, 301.
[13] J. Dong, D. Maestre, C. Conrad-Billroth, T. Juffmann, *J. Phys. D: Appl. Phys.* **2021**, *54*, 394002.
[14] G. Young, P. Kukura, *Annu. Rev. Phys. Chem.* **2019**, *70*, 301.
[15] C.-Y. Cheng, Y.-H. Liao, C.-L. Hsieh, *Nanoscale* **2019**, *11*, 568.
[16] S. Wang, X. Shan, U. Patel, X. Huang, J. Lu, J. Li, N. Tao, *Proc. Natl. Acad. Sci.* **2010**, *107*, 16028.
[17] D. Sevenler, G. G. Daaboul, F. Ekiz Kanik, N. L. Ünlü, M. S. Ünlü, *ACS Nano* **2018**, *12*, 5880.
[18] A. Y. Ozkumur, F. E. Kanik, J. T. Trueb, C. Yurdakul, M. S. Unlu, *IEEE J. Sel. Top. Quantum Electron.* **2019**, *25*, 1.
[19] M. Salina, F. Giavazzi, R. Lanfranco, E. Ceccarello, L. Sola, M. Chiari, B. Chini, R. Cerbino, T. Bellini, M. Buscaglia, *Biosens. Bioelectron.* **2015**, *74*, 539.
[20] R. G. Newton, *Am. J. Phys.* **1976**, *44*, 639.
[21] H. C. van de Hulst, *Light Scattering by Small Particles*, General Publishing Company, Toronto, Canada **1981**.
[22] V. Degiorgio, M. A. C. Potenza, M. Giglio, *Eur. Phys. J. E* **2009**, *29*, 379.
[23] A. D. Snider, A. Garcia-Lopez, *IEEE Trans. Antennas Propag.* **2006**, *54*, 3840.
[24] I. Izeddin, J. Boulanger, V. Racine, C. Specht, A. Kechkar, D. Nair, A. Triller, D. Choquet, M. Dahan, J. Sibarita, *Opt. Express* **2012**, *20*, 2081.
[25] T. D. Canady, N. Li, L. D. Smith, Y. Lu, M. Kohli, A. M. Smith, B. T. Cunningham, *Proc. Natl. Acad. Sci.* **2019**, *116*, 19362.
[26] F. E. Kanik, I. Celebi, D. Sevenler, K. Tanriverdi, N. L. Ünlü, J. E. Freedman, M. S. Ünlü, *Sci. Rep.* **2022**, *12*, 1.
[27] *Handbook of Surface Plasmon Resonance: 2nd Edition*, (Ed.: R. B. M. Schasfoort), Royal Society of Chemistry, London, UK, **2017**.
[28] O. Avci, R. Adato, A. Y. Ozkumur, M. S. Ünlü, *Opt. Express* **2016**, *24*, 6094.
[29] Y. Song, J. Song, X. Wei, M. Huang, M. Sun, L. Zhu, B. Lin, H. Shen, Z. Zhu, C. Yang, *Anal. Chem.* **2020**, *92*, 9895.
[30] A. Schmitz, A. Weber, M. Bayin, S. Breuers, V. Fieberg, M. Famulok, G. Mayer, *Angew. Chem., Int. Ed.* **2021**, *60*, 10279.
[31] F. Giavazzi, M. Salina, R. Cerbino, M. Bassi, D. Prosperi, E. Ceccarello, F. Damin, L. Sola, M. Rusnati, M. Chiari, B. Chini, T. Bellini, M. Buscaglia, *Proc. Natl. Acad. Sci.* **2013**, *110*, 9350.
[32] G. Nava, E. Ceccarello, F. Giavazzi, M. Salina, F. Damin, M. Chiari, M. Buscaglia, T. Bellini, G. Zanchetta, *Phys. Chem. Chem. Phys.* **2016**, *18*, 13395.
[33] R. J. White, N. Phares, A. A. Lubin, Y. Xiao, K. W. Plaxco, *Langmuir* **2008**, *24*, 10513.
[34] M. Soler, L. M. Lechuga, *J. Appl. Phys.* **2021**, *129*, 111102.
[35] D. Gopalan, P. R. Nair, *ACS Sens.* **2020**, *5*, 1374.
[36] J. Fajnzylber, , J. Regan, K. Coxen, H. Corry, C. Wong, A. Rosenthal, D. Worrall, F. Giguel, A. Piechocka-Trocha, C. Atyeo, S. Fischinger, A. Chan, K. T. Flaherty, K. Hall, M. Dougan, E. T. Ryan, E. Gillespie, R. Chishti, Y. Li, N. Jilg, D. Hanidziar, R. M. Baron, L. Baden, A. M. Tsibris, K. A. Armstrong, D. R. Kuritzkes, G. Alter, B. D. Walker, X. Yu, J. Z. Li, *Nat. Commun.* **2020**, *11*, 1.
[37] A. S. Walker, E. Pritchard, T. House, J. V. Robotham, P. J. Birrell, I. Bell, J. I. Bell, J. N. Newton, J. Farrar, I. Diamond, R. Studley, J. Hay, K.-D. Vihta, T. E. A. Peto, N. Stoesser, P. C. Matthews, D. W. Eyre, K. B. Pouwels, COVID-19 Infection Survey team *eLife* **2021**, 10:e64683.
[38] S. Enoki, R. Iino, N. Morone, K. Kaihatsu, S. Sakakihara, N. Kato, H. Noji, *PLoS One* **2012**, *7*, e49208.
[39] N. Li, X. Wang, J. Tibbs, C. Che, A. S. Peinetti, B. Zhao, L. Liu, P. Barya, L. Cooper, L. Rong, X. Wang, Y. Lu, B. T. Cunningham, *J. Am. Chem. Soc.* **2021**, *144*, 1498.
[40] G. G. Daaboul, D. S. Freedman, S. M. Scherr, E. Carter, A. Rosca, D. Bernstein, C. E. Mire, K. N. Agans, T. Hoenen, T. W. Geisbert, M. S. Ünlü, J. H. Connor, *PLOS One* **2017**, *12*, e0179728.
[41] E. Seymour, N. L. Ünlü, E. P. Carter, J. H. Connor, M. S. Ünlü, *ACS Sens.* **2021**, *6*, 229.
[42] L. Vanjur, T. Carzaniga, L. Casiraghi, G. Zanchetta, F. Damin, L. Sola, M. Chiari, M. Buscaglia, *Polymers* **2021**, *13*, 3897.
[43] D. G. Lowe, *Int. J. Comput. Vis.* **2004**, *60*, 91.
[44] S. Delbue, S. D'Alessandro, L. Signorini, M. Dolci, E. Pariani, M. Bianchi, S. Fattori, A. Modenese, C. Galli, I. Eberini, P. Ferrante, *Emerging Microbes Infect.* **2021**, *10*, 252.